# Utilizing the MicroASAR on the SIERRA UAS for NASA's Characterization of Arctic Sea Ice Experiment

Evan Zaugg[a,b], David Long[a], Matthew Edwards[b], Matthew Fladeland[c], Richard Kolyer[c], Ian Crocker[d], James Maslanik[d], Ute Herzfeld[e] and Bruce Wallin[e]

[a]Brigham Young University, 459 CB, Provo, UT 84602, USA
[b]ARTEMIS Inc., 36 Central Ave, Hauppauge, NY 11788, USA
[c]NASA Ames Research Center, MS 245-4 Moffett Field, CA 94035, USA
[d]University of Colorado, CCAR, Boulder, CO, 80309, USA
[e]University of Colorado, CIRES, Boulder, CO, 80309, USA

## ABSTRACT

The MicroASAR is a flexible, robust SAR system built on the successful legacy of the BYU $\mu$SAR. It is a compact LFM-CW SAR system designed for low-power operation on small, manned aircraft or UAS. The NASA SIERRA UAS was designed to test new instruments and support flight experiments. NASA used the MicroASAR on the SIERRA during a science field campaign in 2009 to study sea ice roughness and break-up in the Arctic and high northern latitudes. This mission is known as CASIE-09 (Characterization of Arctic Sea Ice Experiment 2009). This paper describes the MicroASAR and its role on the SIERRA UAS platform as part of CASIE-09.

**Keywords:** SAR, MicroASAR, UAS, NASA SIERRA, Arctic, Sea Ice

## 1. INTRODUCTION

Synthetic aperture radar (SAR) is a useful tool in a variety of surveillance and remote sensing applications. Different SAR systems are designed to meet the varying requirements of different projects. The MicroASAR is a sensor which builds on the design of the BYU $\mu$SAR,[1] but is a much more robust and flexible system.[2] The C-band MicroASAR is a complete, self-contained SAR system that has been designed specifically to be small and lightweight while still being robust and capable. These characteristics make it an ideal SAR system for use on unmanned aircraft systems (UAS) and other small aircraft.

The NASA SIERRA (Sensor Integrated Environmental Remote Research Aircraft) UAS[3] is a medium class, medium duration aircraft designed by the Naval Research Laboratory to test new instruments and support NASA earth science flight experiments. The SIERRA is ideal for deployment in remote areas where manned flight is dangerous. The aircraft has the capacity to carry multiple payloads, which makes it a suitable platform for many different types of missions.

The Characterization of Arctic Sea Ice Experiment 2009 (CASIE-09) combines different remote sensing methods, including satellite observations and UAS, to provide fundamental new insights into ice roughness on the scale of meters to tens of meters. These observations are made in the context of larger-scale environmental forcing. Additionally, the mission offers a technological and operational testbed to demonstrate the value of autonomous vehicles for long-range, long-duration remote sensing science. Five science flights covering 2923 km of sea ice were flown in July 2009.

This paper is organized into three parts. Section 2 summarizes the design of the MicroASAR, section 3 covers its integration onto the NASA SIERRA UAS, and section 4 explains its role in the CASIE mission.

Further author information (by affiliated organization):
BYU: zaugg@mers.byu.edu
ARTEMIS Inc.: matt@artemisinc.net
NASA Ames: matthew.fladland@nasa.gov
UC CCAR: roger.crocker@colorado.edu
UC CIRES: herzfeld@tryfan.colorado.edu

Radar Sensor Technology XIV, edited by Kenneth I. Ranney, Armin W. Doerry, Proc. of SPIE Vol. 7669, 76690Z · © 2010 SPIE · CCC code: 0277-786X/10/$18 · doi: 10.1117/12.850230

Table 1. **MicroASAR System Specifications**

| | |
|---|---|
| **Physical Specifications** | |
| Transmit Power | 30 dBm |
| Supply Power | < 35 W |
| Supply Voltage | +15 to +26 VDC |
| Dimensions | 22.1x18.5x4.6 cm |
| Weight | 2.5 kg |
| **Radar Parameters** | |
| Modulation Type | LFM-CW |
| Operating Frequency Band | C-band |
| Transmit Center Frequency | 5428.76 MHz |
| Signal Bandwidth | 80-200 MHz (variable) |
| PRF | 7-14 kHz (variable) |
| **Radar Operating Specifications** | |
| Theoretical Resolution | 0.75 m (@ 200 MHz BW) |
| Operating Altitude | 500-3000 ft |
| Max. Swath Width | 300-2500 m (alt. dependent) |
| Operating Velocity | 10-150 m/s |
| Collection Time (for 10GB) | 30-60 min (PRF dependent) |
| **Antennas (2 required)** | |
| Type | 2 x 8 Patch Array |
| Gain | 15.5 dB |
| Beamwidth | 8.5°x50° |
| Size | 35x12x0.25 cm |

## 2. MICROASAR DESIGN

The MicroASAR system specifications are summarized in Table 1. The system uses a linear frequency-modulated continuous-wave (LFM-CW) chirp generated by a direct digital synthesizer (DDS) chip. An LFM-CW system is able to maintain a high SNR while transmitting with a lower peak power than a comparable pulsed SAR because the chirp length is maximized. Upon receive, the return signal is mixed with a copy of the transmitted signal in a process known as dechirping. The result of the dechirping is the frequency difference betweent the transmitted and received signals. This difference corresponds directly to the slant-range from the antenna to a target. The bandwidth of the dechirped signal is much lower than the bandwidth of the transmitted signal, so that the required sample rate is lower.

Both the width of the swath that can be imaged by the sensor and the operational platform height are limited by the use of the dechirp scheme of the continuous-wave system. The imaging capabilities of the MicroASAR make it a suitable sensor for operation on small, low-flying aricraft.

The LFM-CW SAR system requires a bistatic configuration with a separate antenna for the receive channel because it is constantly transmitting. An undesirable side effect of bistatic operation is feedthrough between the transmit and receive antennas. This relatively strong feedthrough component dominates the low end of the dechirped spectrum and must be removed before final processing. The MicroASAR accomplishes this in the RF hardware by utilizing a bandpass filter with high out-of-band rejection, as described in.[2] In the dechirp stage, the mix-down signal is offset in frequency such that the resulting dechirped signal is at an intermediate frequency. Rejection of the feedthrough component is accomplished by a surface acoustic wave (SAW) filter with a null at the frequency that corresponds to the feedthrough.

The MicroASAR is completely contained in one aluminum enclosure measuring 22.1x18.5x4.6 cm. Despite its solid metal enclosure, the entire system, including two antennas, weighs less than 3.3 kilograms. A simplified block diagram showing the major signal paths is given in Fig. 1. To maintain phase coherence, all signals and clocks are derived from a single temperature compensated crystal oscillator (TCXO). The DDS generates

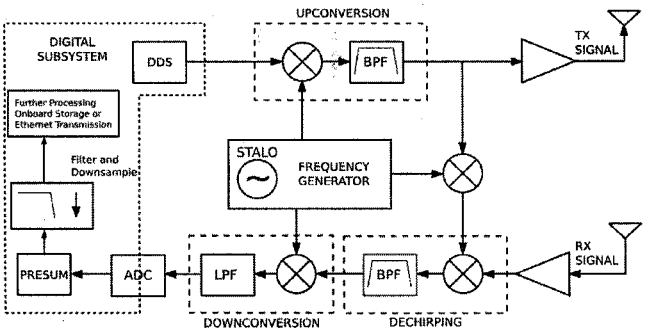


Figure 1. Simplified block diagram for the MicroASAR system. All clocks and signals are derived from the temperature compensated crystal oscillator (TCXO).

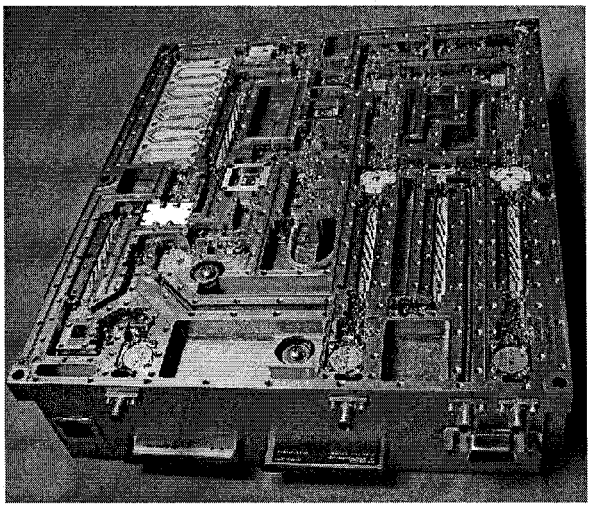

Figure 2. MicroASAR with cover removed showing RF components. Also pictured is the front panel containing RF ports, flash memory cards, serial and ethernet connections.

the LFM chirp, which is then up-converted, amplified, and transmitted. A copy of this transmitted chirp is frequency-shifted and mixed with the received signal to produce the dechirped signal. The dechirped signal is then downconverted to an offset video frequency and sampled.

The MicroASAR's digital subsystem contains a DDS chip which is used to generate the LFM chirp, an ADC, and an FPGA. The FPGA controls the other chips and performs simple, pre-storage processing such as presumming and filtering. Because the dechirped radar data is sampled at an offset video frequency, it is necessary to filter and downsample in order to obtain baseband data for storage. The digitized signal is either streamed through the Ethernet interface or written to two flash memory cards, which are accessible through the front panel of the system.

LFM-CW operation requires less power than a comparable pulsed SAR and enables hardware which is less complicated. The hardware solution provided by Artemis, Inc., (shown in Fig. 2), is robust enough to withstand the rigors of airborne applications while still being small and lightweight.

## 3. IMAGING FROM THE SIERRA

The NASA SIERRA UAS is an ideal platform for the MicroASAR (see Figs. 3 and 4). A large payload capacity, efficient mission planning software and in-flight programmable autopilot make the SIERRA a perfect vehicle for

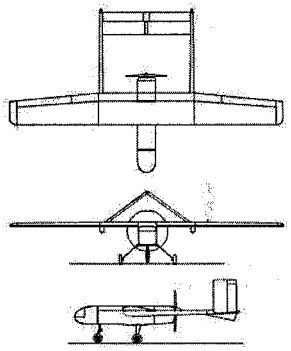

| | |
|---|---|
| Wing Span | 20 ft. |
| Length | 11.8 ft. |
| Height | 4.6 ft. |
| Wing Area | 42.4 sq. ft. |
| Empty Weight | 215 lbs. |
| Gross Weight | 345 lbs. |
| Max Speed | 79 kts. |
| Cruise Speed | 55 kts. |
| Stall Speed (clean) | 30 kts. |
| Aspect ratio | 9.43 |
| Rate of Climb | 545 ft./min. |
| CG Position | 29-32% Chord |
| Payload weight | ~100lbs |

Figure 3. NASA SIERRA UAS 3-View and Specifications

a variety of data gathering missions. The SIERRA UAS is of particular value when long duration flights preclude a human pilot, or in a remote, harsh environment which would put pilots and manned aircraft at risk.

Like other UAS of its class, the SIERRA can fly long distances at low altitudes while providing high maneuverability and relatively slow velocities. However, unlike smaller UAS, the SIERRA is particularly well-suited for the CASIE project, because of its larg payload capacity, significant flight range, ready availability, and reasonable deployment costs. A combination of sensors were deployed that would have been too large and heavy to deploy on a single, smaller UAS. This large payload is critical to meeting our need for acquiring simultaneous sea ice observations from multiple sensors. The requirement for making simultaneous measurements is driven by the fact that the ice pack in Fram Strait is highly dynamic, with fast ice drift and potential for ridging and rafting between flights.

For the CASIE

- Laser altimeter/surface height profiler (non-scanning) system consisting of two lasers acquiring simultaneous but laterally offset laser tracks, GPS, inertial measurement unit, and payload computer.
- Imaging synthetic aperture radar (the MicroASAR) with video camera.
- Three digital cameras.
- Up-looking and down-looking broadband shortwave radiation pyranometers.
- Up-looking and down-looking shortwave spectrometers.
- Down-looking temperature sensors (pyrometers).
- Temperature/Rh Sensors

## 4. THE CASIE MISSION

The CASIE mission was conducted as a data collection effort in support of an International-Polar-Year project titled "Sea Ice Roughness as an Indicator of Fundamental Changes in the Arctic Ice Cover: Observations, Monitoring, and Relationships to Environmental Factors." This project is supported by NASA Cryospheric Sciences and led by the investigator team J. Maslanik (CU Boulder, PI), U. Herzfeld (CU Boulder), J. Heinrichs (Ft. Hays State University), R. Kwok (JPL) and D. Long (Brigham Young University, Provo). The purpose of the CASIE mission is to determine the degree to which ice-roughness monitoring via remote sensing can detect basic changes in ice conditions such as ice thickness and ice age, to investigate relationships between ice roughness and factors affecting the loss or maintenance of the perennial ice cover, and to determine how roughness varies as a function of different kinematic conditions and ice properties.

Figure 4. The NASA SIERRA UAS and the CASIE team in Ny-Alesund, Svalbard, Norway.

CASIE contributes to the overall IPY project by providing an unprecedented suite of high-resolution data over a range of sea ice conditions within the Fram Strait region between northern Greenland and Svalbard. These data include surface topography observations, standard electro-optical (EO) imagery, SAR imagery, and surface reflectance/temperature measurements. Matthew Fladeland of the NASA Ames Research Center led the CASIE mission. NASA deployed the SIERRA with the MicroASAR on-board, a ground control station, a science team, and an operation and logistics team to collect science data in and around the Svalbard archipelago of Norway in July 2009.

Flights of the SIERRA originated from Ny-Alesund, Svalbard. This location was selected because it was within acceptable flight range of ice with a range of thicknesses, age, and ridging characteristics. The SIERRA typically flew to the north and northwest, passing over open ocean and the marginal sea ice zone to target the variety of thick, old ice within the Fram Strait ice outflow region. Once over the desired ice conditions, most flight patterns involved closely spaced, adjacent flight tracks to provide good mapping coverage. The five science flights are summarized here:

- July 16 - 5hr, 49min
- July 22 - 7hr, 57min
- July 24 - 10hr, 7min
- July 27 - 8hr, 39min
- July 29 - 8hr, 15min
- 2923 km of sea ice flown

### 4.1 CASIE Research Questions and Data Collection

Recent observations and modeling studies[4–7] suggest large decreases in Arctic sea-ice thickness in recent years. Uncertainty remains, however, concerning overall loss of ice mass versus redistribution of mass within the Arctic Basin. "Ridging and rafting" of the ice cover, where ice is piled up due to compression of the ice pack, is one mechanism for such mass redistribution. If the ice pack is undergoing fundamental changes, such as a shift to a largely seasonal sea-ice cover, other related changes in properties are likely to be observed. Ridging characteristics, changes in frequency of rafting versus ridging, the responses of the pack to pressure forces, and momentum exchange between ice, atmosphere and ocean could be expected to vary over time. In turn, changes

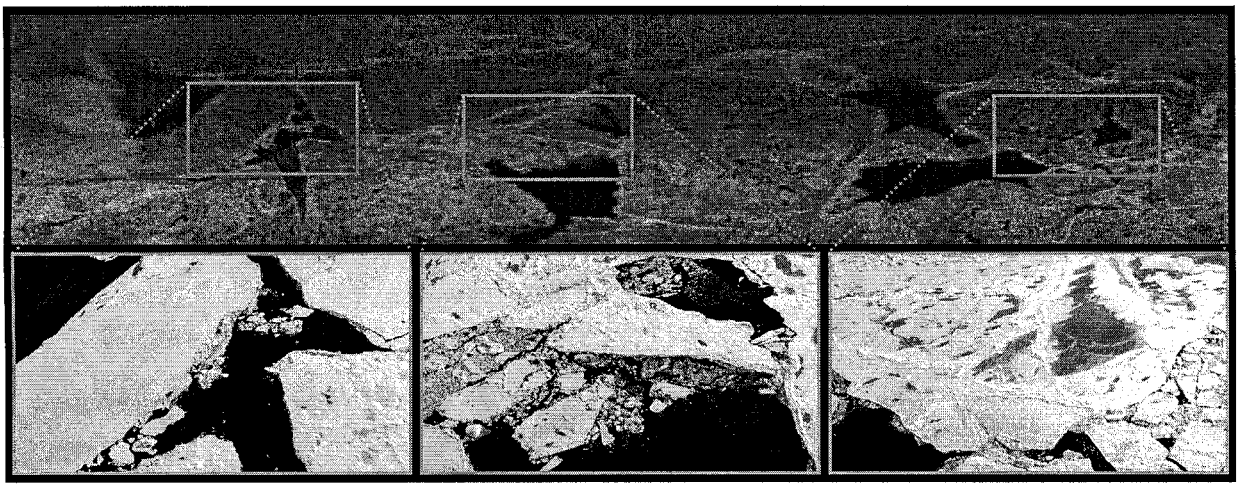

Figure 5. A series of images collected during the CASIE mission showing agreement between the MicroASAR sensor (top) and the on board video camera (bottom).

in these ice topography and related roughness conditions affect dynamic and thermodynamic properties. The degree to which such changes might act as positive or negative feedbacks for ice growth is unknown.

Our project's research combines a variety of remote sensing methods, including satellite observations and UAS, to provide fundamental new insights into ice roughness on the scale of meters to tens of meters in the context of larger-scale environmental forcings. Our intent is to be able to relate scattering and emission properties to surface roughness and hence to geophysical properties that are difficult or impossible to observe directly. Fine scale and in situ observations are essential to understanding physical processes at work, but it is necessary to know how processes aggregate over the scale of the types of spaceborne observations that we must rely upon for regional and hemispheric-scale monitoring.

The approach we are using combines high-resolution aerial observations with satellite data and forward modeling to document the characteristics and evolution of ice roughness over a range of space and time scales. With this information in hand, we can interpret roughness in terms of other ice conditions, improve our understanding of effects on overall ice mass, and develop climate model parameterizations to better simulate sea ice conditions.

A key aspect of CASIE is that it provides data at finer spatial resolution than previously obtained, over difficult to access locations in the high Arctic. Satellites cannot provide the desired simultaneous combination of sensor types and resolution. Piloted aircraft typically fly too high and too fast to yield the fine-scale sampling rates and mapping patterns required by our project. For the science flights, the SIERRA typically flew less than 1000 feet above the ice while simultaneously collecting data from the MicroASAR and the other payload sensors.

## 4.2 MicroASAR Data Processing and Analysis Approaches

The MicroASAR data was stored onto Compact Flash cards and processed post flight. SAR images were formed using the Range-Doppler algorithm. The SAR imagery, as in Figs. 5 and 6, covers a swath of sea ice about 850 meters wide with a range resolution of about 90 cm.

SAR is useful for operating in the polar regions, because the radar signal penetrates thick and thin cloud covers. The SAR signal is affected by volume and surface scattering at several scales, which are manifested in sea ice features, including ridges, rubbles, and thickness and density variations. Information on the roughness and structure of sea ice can be derived from the thickness and spatial distribution of the snow cover on top of the sea ice.[8,9] Although the snow cover is largely penetrated by the MicroASAR signal, inferring sea-ice roughness from snow-thickness variability is not necessary, as reflections most likely come from near the sea-ice/snow interface.

The geostatistical classification method[10] is applied here to identify and discriminate sea-ice properties and sea-ice types based on spatially averaged differences in SAR backscatter intensity. The term "geostatistical

classification" summarizes a suite of methods and tools for automated characterization and classification of physical properties from irregularly or regularly distributed spatial data as commonly result from remote-sensing observations. Within the geostatistical interpolation methods, the classification approach shares only the notion of spatial continuity and its analysis through some form of spatial structure function.[10,11]

As a consequence of the side-looking illumination of the sea-ice surface, the received signal intensity falls off from the near-field to the far-field in across-track direction (see panels a and b in Fig. 6). In general, limitations in the spatial calibration of SAR data preclude its use with many multivariate statistical methods common in satellite image analysis.[12] Instead, an analysis method that operates in a differential domain is needed. The geostatistical characterization and classification[8,10] method meets this requirement by analyzing vario-functions.[13] The first-order vario function is defined as

$$v_1(h) = \frac{1}{2n}\sum_{i=1}^{n}[z(x_i) - z(x_i+h)]^2 \tag{1}$$

for pairs of points $(x_i, z(x_i)), (x_i+h, z(x_i+h)) \in \mathcal{D}$, where $\mathcal{D}$ is a region in $\mathcal{R}^2$ (case of survey profiles) or $\mathcal{R}^3$ (case of survey areas) and $n$ is the number of pairs separated by $h$.

The definition of the first-order vario function already incorporates differences, and higher-order functions are designed to compensate for slopes and errors in the received data.

The second-order vario function $v_2$, termed *varvar function*, is defined as

$$v_2(k) = \frac{1}{2s}\sum_{j=1}^{s}[v_1(h_j) - v_1(h_j+k)]^2 \tag{2}$$

with $((h_j, v_1(h_j)), (h_j+k, v_1(h_j+k))) \in \mathcal{V}_1 = (h, v_1(h))$, the first-order vario-function set. Higher-order vario functions are defined recursively, following an analogy to Eq. 2

Parameters that may be extracted from vario functions in automated routines can be associated to spatial roughness properties of the sea ice. The parameters may be used individually or in combination in feature vectors that may be input into deterministic or connectionist class association algorithms (see[12] for a neural net application and[8] for characterization of sea-ice roughness identified by snow on ice).

Examples of parameters are (from left to right in Fig. 6, panel c,d,e,f): Parameter *pond* is defined as the maximum value in the vario function (in the operation window) and relates to overall roughness (in the window). Spatial surface roughness as summarized by *pond* is directly related to atmospheric roughness length as used in boundary layer meteorology (resistance to wind).[8] Parameter *mindist*, defined as the average size of the dominant spatial features in the window, works to quantify sea-ice features such as the characteristic spacing of leads or ridges, or the average size of rubbles in a sea-ice rubble field. Parameter $p1$ uses absolute size, whereas parameter $p2$ uses relative size, thereby mapping relative significance of spatial features (significance relative to the size of the features). Parameters can be calculated directionally or globally, to assure independence of direction of the flight track to direction of oceanic currents, ice floes or wind, which are morphogenetic causes of sea-ice changes.

The panels in Fig. 6 show parameters derived for a single MicroASAR data set. After optimal processing/correction of MicroASAR data, the classification will be applied to the entire set of SAR data along the flight track, by (1) deriving location-dependent functionals of parameters, (2) combining those into location-dependent feature vectors, and (3) assigning sea-ice classes along the MicroASAR survey tracks.

A problem in analysis and classification of satellite SAR data is the identification of sea-ice types, including identificaiton of open water versus thin ice or brash ice coverage. Automated classification of sea ice provinces from SAR data has been undertaken successfully,[14–17] however the problem of ground-validating prototype ice classes is complicated by a lack of coincidental observations, as field observations of sea-ice properties are uncommon. The simultaneously collected MicroASAR and video data from the CASIE experiment (see Fig. 5) provide a unique source for SAR-data validation.

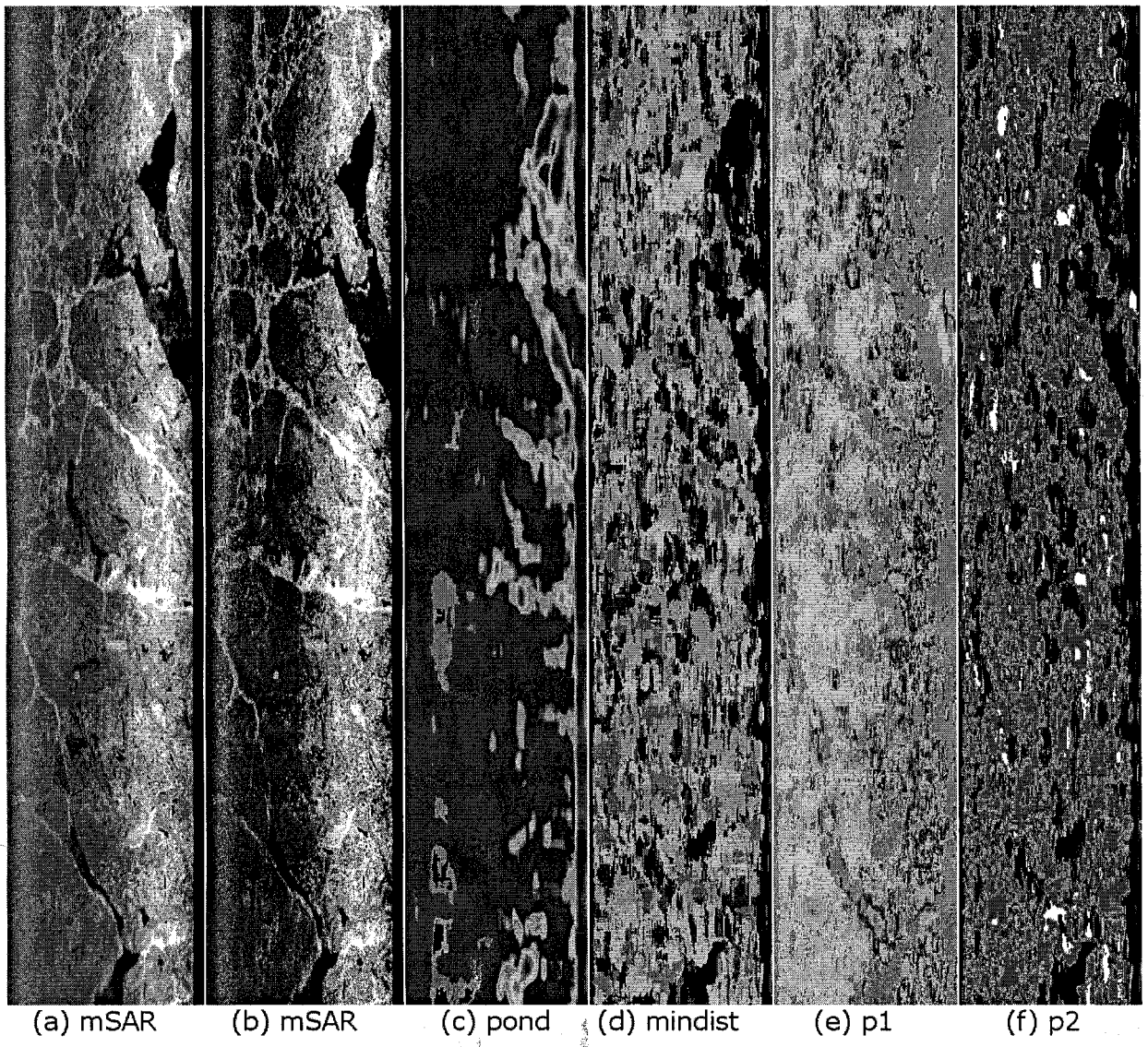


Figure 6. Example of MicroASAR data set from the CASIE experiment collected 27 July, 2010. The backscatter values and spatial roughness parameters are shown. The data shows sea ice floes with leads and variable roughness throughout the imaged area. From left to right: (a) Greyscale backscatter intensity. (b) Color-enhancement of (a) to visually improve differentiation of surface reflectance properties. (c)-(f) are vario-parameters derived by application of geostatistical classification algorithms. (c) *pond* parameter (overall roughness), (d) *mindist* parameter (average size/ spacing of significant spatial features). (e) parameter $p1$ absolute significance of spatial features (as found by *mindist*). (f) parameter $p2$ (relative significance of spatial features, as found by *mindist*). A more detailed explanation is in the text.

## 5. CONCLUSION

With the successful collection of science data for the CASIE project, the value of a UAS-borne, small synthetic aperture radar has been demonstrated. The compact, flexible design of the MicroASAR made it ideal for deployment on this mission. Using the MicroASAR on the SIERRA has opened the way for many other applications that would be well served by utilizing a small SAR on a UAS.

## REFERENCES


[1] E.C. Zaugg, D.L. Hudson, and D.G. Long, "The BYU $\mu$SAR: A Small, Student-Built SAR for UAV Operation", in *Proc. Int. Geosci. Rem. Sen. Symp.*, Denver Colorado, pp.411-414, Aug. 2006.

[2] M. Edwards, D. Madsen, C. Stringham, A. Margulis, and B. Wicks, "MicroASAR: A Small, Robust LFM-CW SAR for Operation on UAVs and Small Aircraft", in *Proc. Int. Geosci. Rem. Sen. Symp.*, Boston, Mass, July, 2008.

[3] Fladeland, M. M., Berthold, R., Monforton, L., Kolyer, R., Lobitz, B., & Sumich, M., "The NASA SIERRA UAV: A new unmanned aircraft for earth science investigations", American Geophysical Union, Fall Meeting 2008, abstract B41A-0365.

[4] J.A. Maslanik, C. Fowler, J. Stroeve, S. Drobot, J. Zwally, D. Yi, and W. Emery, "A younger, thinner Arctic ice cover: Increased potential for rapid, extensive sea-ice loss," *Geophysical Research Letters*, vol. 34, L24501, 2007.

[5] M.C. Serreze, M. Holland, and J. Stroeve, "Perspectives on the Arctic's shrinking sea-ice cover", *Science*, Vol. 315, No. 5818, pp. 1533-1536, March 2007.

[6] J. Stroeve, M. Serreze, F. Fetterer, T. Arbetter, W. Meier, J. Maslanik, and K. Knowles, "Tracking the Arctic's shrinking sea-ice cover: Another extreme September minimum in 2004", *Geophys. Res. Lett.* Vol. 32, No. 4, Feb. 2005.

[7] J. Stroeve, M. Holland, W. Meier, T. Scambos, and M. Serreze, "Arctic sea ice decline: Faster than forecast", *Geophys. Res. Lett.*, Vol. 34, May 2007.

[8] U.C. Herzfeld, J. Maslanik and M. Sturm, "Geostatistical characterization of snow-depth structures on sea ice near Point Barrow, Alaska — A contribution to the AMSR-ICE03 Field Validation Campaign", *IEEE Transactions on Geoscience and Remote Sensing*, vol. 44, no. 11 , p. 3038-3056, Nov. 2006.

[9] J.A. Maslanik, M. Sturm, M. Belmote Rivas, A.J. Gasiewski, J.F. Heinrichs, U.C. Herzfeld, J. Holmgren, M. Klein, T. Markus, D.K. Perovich, J.G. Sonntag, J.C. Stroeve, and K. Tape, "Spatial Variability of Barrow-Area Shore-Fast Sea Ice and Its Relationships to Passive Microwave Emissvity", *IEEE Trans. Geosci. Remote Sensing*, vol. 44, no. 11, pp. 3021-3031, Nov. 2006.

[10] U.C. Herzfeld, "Master of the Obscure — Automated Geostatistical Classification in Presence of Complex Geophysical Processes", *Mathematical Geosciences*, v. 40, p. 587-618, July 2008.

[11] U.C. Herzfeld, "Least squares collocation, geophysical inverse theory, and geostatistics: A bird's eye view", *Geophysical Journal International*, vol. 111, no. 2, p. 237-249, 1992.

[12] U.C. Herzfeld, and O. Zahner, "A connectionist-geostatistical approach to automated image classification, applied to the analysis of crevasse patterns in surging ice", *Computers & Geosciences*, vol. 27, p. 499-512, June 2001.

[13] U.C. Herzfeld, "Vario-functions of higher order — definition and application to characterization of snow surface roughness", *Computers & Geosciences*, vol. 28, no. 5, p. 641–660, June 2002.

[14] J. Karvonen, "Baltic Sea ice SAR segmentation and classification using modified pulse-coupled neural networks", *IEEE Trans. Geoscience and Remote Sensing*, vol. 42, no. 7, pp. 1566-1574, July 2004.

[15] J. Karvonen, "Compaction of C-band Synthetic Aperture Radar based sea ice information for navigation in the Baltic Sea", *Helsinki University of Technology Dissertations in Computer and Information Science*, Report D17, 162, Dec. 2006.

[16] J. Karvonen and A. Kaarna, "Sea Ice SAR Feature Extraction by Non-Negative Matrix and Tensor Factorization", in *Proc. Geoscience and Remote Sensing Symposium*, Vol. 4, pp.1093-1096), Boston, Mass., July 2008.

[17] U.C. Herzfeld, S. Williams, J. Heinrichs, J. Maslanik, and S. Sucht, "Geostatistical and statistical approaches to automated classification of sea-ice properties and provinces from SAR data, with applications to ice environments near Point Barrow, Alaska," *Mathematical Geosciences*, 2009.